Moroccan Journal of Chemistry
ISSN : 2351-812X

Mor. J. Chem., 2023, Volume 11, Issue 3, Page 780-801
https://revues.imist.ma/index.php/morjchem
https://doi.org/10.48317/IMIST.PRSM/morjchem-v11i3.40959

Nano-Yttrium Titanate Coated 304 Stainless Steel: Preparation, Characterization and Corrosion Protection Application

Soliman H. A. *, Ibrahim M. M., Ali L. I., Saif M., Abdelshafi N. S., Khaled K. F.
Electrochemistry Research Laboratory, Chemistry Department, Faculty of Education, Ain Shams University, Roxy, 11711, Cairo, Egypt
**Corresponding author, Email address: hananatef@edu.asu.edu.eg*

Received *8 June 2023,*
Revised *04 July 2023,*
Accepted *04 July 2023*

Citation*: Soliman H. A., Ibrahim M. M., Ali L. I., Saif M., Abdelshafi N. S., Khaled K. F. (2023) Nano-Yttrium Titanate Coated 304 Stainless Steel: Preparation, Characterization and Corrosion Protection Application, Mor. J. Chem., 14(3), 780-801*

Abstract: A study was conducted to develop a protective nano-coating for 304 stainless steel in acidic conditions (1.0 M HCl) using nano-yttrium titanate. The nano-yttrium titanate ($Y_2Ti_2O_7$) was synthesized through a spin coating sol-gel method at various calcination temperatures. The coated 304 stainless steel samples were subjected to characterization using different surface analysis techniques, including X-ray diffraction analysis (XRD), atomic force microscopy (AFM), scanning electron microscopy (SEM), and energy dispersive X-ray analysis (EDS). The XRD analysis confirmed the formation of the desired $Y_2Ti_2O_7$phase at 700 °C, which remained stable up to 900 °C with the highest intensity. AFM results revealed that the $Y_2Ti_2O_7$-coated steel samples calcinated at 900 °C exhibited lower roughness parameters (R_a = 9.4 nm and R_{rms} = 11.7 nm) compared to the uncoated steel samples treated with HCl (R_a = 18.8 nm and R_{rms} = 22.7 nm), indicating effective surface protection. SEM images also supported these findings. Furthermore, electrochemical techniques such as Tafel polarization, electrochemical frequency modulation, and electrochemical impedance spectroscopy were employed. Consistently, all three techniques demonstrated that increasing the calcination temperature and the presence of the $Y_2Ti_2O_7$phase improved the inhibition efficiency (η%) against corrosion in 1.0 M HCl. The inhibition efficiency reached its maximum value of approximately 99.6% at 900 °C. Overall, the study's findings highlight the significant enhancement of corrosion inhibition efficiency in 304 stainless steel achieved through the application of a nano-yttrium titanate coating. This improvement is attributed to the coating's hydrophobic properties, as evidenced by contact angle measurements.

Keywords: Nano-coating; Sol-gel; $Y_2Ti_2O_7$; Stainless steel; Corrosion; Electrochemical frequency modulation; Electrochemical Impedance spectroscopy; Tafel polarization

1. Introduction

Coating is a valuable method for controlling the corrosion of 304 stainless steel in aqueous environments (Huh *et al.*, 2005, Lopez *et al.*, 2005, Buyuksagis *et al.*, 2015, Xin *et al.*, 2019, Omar *et al.*, 2017). 304 stainless steel is the most versatile and widely used stainless steel, with extensive applications in industries such as aerospace, petroleum, and chemical manufacturing. Despite its widespread use, it is susceptible to various forms of corrosion in different aggressive environments (Nazeri *et al.*, 1997, Ivankovic *et al.*, 2016, Samim *et al.*, 2020, Perez *et al.*, 2002, Boudalia *et al.*,

2013, Eziuka *et al.*, 2023). One of the most aggressive environments is hydrochloric acid, which is commonly used in acid pickling, industrial acid cleaning, and acid descaling processes (Hooshmand Zaferani *et al.*, 2013, Yue *et al.*, 2023, Li *et al.*, 2005, Li *et al.*, 2008, El-Haddad and Elattar, 2013, Pantoja *et al.*, 2019, Verma *et al.*, 2020, Onyeachu *et al.*, 2022, Aslam *et al.*, 2022, Itodoh *et al.*, 2023, Salim *et al.*, 2023, El Ouadi *et al.*, 2017). Ceramic coatings are recommended as effective barriers against corrosion in aqueous environments. These coatings, especially nano-structured ceramics, exhibit good passivity, low conductivity, and excellent protection properties (Curkovic *et al.*, 2013, Movassagh-Alanagh and Mahdavi, 2020, Boukerche *et al.*, 2019, Ramaprakash et *al.*, 2016). Various ceramic coatings, such as TiO_2, SiO_2, Al_2O_3, ZrO_2 and mixed oxides like ZnO/TiO_2 and ZrO_2-TiO_2 have been used to protect stainless steel in different corrosion conditions (Curkovic *et al.*, 2013, Perez *et al.*, 2002, Chen *et al.*, 2011a, Di Maggio *et al.*, 1996, Boukerche *et al.*, 2019, Mohan *et al.*, 2020, Ziouche *et al.*, 2021). Yttrium titanate, an important pyrochlore ceramic with the formula $A_2B_2O_7$, is utilized as a protective material (D'Isanto *et al.*, 2021, Zhao *et al.*, 2020, Behnamian *et al.*, 2017) in thermal barrier coatings (TBCs) widely used in various industries (Nguyen *et al.*, 2020).

In this study, we aimed to investigate the corrosion resistance ability of nano-structured $Y_2Ti_2O_7$-coated 304 stainless steel, specifically in relation to its application in the petroleum industry. The petroleum industry involves various processes, including acid pickling, industrial acid cleaning, and acid descaling, where 304 stainless steel is exposed to hydrochloric acid (HCl) as a corrosive medium. As an attempt to protect the steel from the corrosive effects of hydrochloric acid, we applied a nano-structured $Y_2Ti_2O_7$ coating and evaluated its corrosion resistance using electrochemical techniques, including electrochemical frequency modulation (EFM), electrochemical impedance spectroscopy (EIS), and Tafel polarization. For this initial investigation, a concentration of 1.0 M HCl was used to assess the coating's ability to resist corrosion. This serves as a starting point, and further studies can be conducted to explore the performance of the coating in more aggressive environments and assess its potential for extended protection.

2. Experimental Details

2.1 Sourcing and preparation of $Y_2Ti_2O_7$ coated stainless steel

Austenitic stainless steel plates (304) with dimensions of 10 x 25 x 1 mm were employed as the substrates. Prior to the application of the coating, the substrates underwent a series of mechanical polishing steps utilizing SiC abrasive papers of various grit sizes, namely 320, 400, 600, 800, 1200, 1500, and 2000. Afterward, the substrates were subjected to ultrasonic cleaning for 10 minutes each, using acetone, ethanol, and distilled water, respectively, and followed by thorough drying.

The $Y_2Ti_2O_7$ film was prepared by using yttrium nitrate (0.250 g) and titanium tetra isopropoxide (TTIP; 0.300 mL) as precursors for Y and Ti, respectively. These precursors were dissolved in a mixture of methanol (5.00 mL), water (0.130 mL) and HCl (0.016 mL) (Saif *et al.*, 2015). The mixture was stirred for 10 minutes and immediately spin-coated onto the surface-prepared stainless steel 304 substrates at 3000 rpm for 1 minute. The coated substrates were subsequently dried at 80 °C for 45 minutes. To investigate the impact of calcination temperature on the anti-corrosion behavior of the prepared coatings, the coated substrates were subjected to calcination at various temperatures (400, 500, 600, 700, 800, 900, 1000 °C) for 2 hours. Titanium tetra isopropoxide (TTIP) with the chemical formula $Ti[O(C_3H_7)]_4$ was obtained from ACROS (USA), while $Y(NO_3)_3$ was prepared by reacting Y_2O_3 obtained from Aldrich with nitric acid from Merk. Methanol, hydrochloric acid, and acetic acid were purchased from Sigma-Aldrich.

2.2 Electrochemical measurements

Samples of 304 stainless steel, both coated and uncoated, were mounted in Teflon holders, exposing a surface area of 1 cm^2. Electrochemical measurements were performed using a standard three-compartment glass cell setup. The stainless steel specimen served as the working electrode (WE), while a platinum mesh was used as the counter electrode (CE). The experiment employed a saturated calomel electrode (SCE) as the reference electrode. Fritted glass was used to separate the counter electrode from the working electrode compartment, and a Luggin capillary was connected to the reference electrode to minimize IR drop effects. Prior to initiating the measurements, the electrode potential was allowed to stabilize for 60 minutes at room temperature (25°C ±1). All electrochemical measurements were carried out using a Gamry 3000 Instrument Potentiostat/Galvanostat/ZRA, which was connected to a personal computer for data collection. Data analysis and visualization were performed using the Echem Analyst 6.33 software, along with specific Gamry applications such as EFM140 for EFM, EIS300 for EIS, and dc105 for dc corrosion (Tafel) measurements. Electrochemical frequency modulation (EFM) was performed using two frequencies: 2.0 and 5.0 Hz, with a base frequency of 0.1 Hz, and a perturbation signal amplitude of 10 mV for both frequencies. Electrochemical impedance spectroscopy (EIS) measurements were conducted by applying a small alternating voltage perturbation with a peak-to-peak amplitude of 10 mV over a frequency range of 100 kHz to 20 mHz. For Tafel measurements, the electrode potential was scanned from -250 to 250 mV at the open circuit potential, using a scan rate of 5mV/s (Abdelshafi *et al.*, 2022a, Abdelshafi *et al.*, 2022b, Salhi *et al.*, 2016, Almashhdani and Alsaadie, 2018, Sikine *et al.*, 2018). The inhibition efficiency of the $Y_2Ti_2O_7$ coated steel at different calcination temperatures was calculated using the EFM and Tafel techniques, represented as η_{EFM} % and η_{Tafel} %, respectively. These efficiencies were calculated by the following equation:

$$\eta_{EFM} \text{ or } \eta_{Tafel}\% = (1- \frac{i_{corr}}{i^o_{corr}}) \times 100$$

i^o_{corr} and i_{corr} are corrosion current density in the absence and presence of the coating, respectively. The inhibition efficiency calculated from EIS technique, represented as η_{EIS} % followed the equation:

$$\eta_{EIS}\% = (1 - \frac{R^o_P}{R_P}) \times 100$$

R^o_P and R_P are the polarization resistances in the absence and presence of the coating, respectively.

2.3 Surface analysis

X- ray diffraction patterns of coated samples were recorded using a Pert Philips X-ray diffraction (XRD) instrument with Cukaα radiation, operating at 40 kV and 30 mA and scan rate of 50 min^{-1}. The surface topography was investigated using atomic force microscopy (AFM) technique with a Nano surf C3000 instrument (Nano surf AG, Graubernstr 12, CH-4410 Liestal – Switzerland). The images were acquired in phase contrast mode using NCLR cantilever type with a spring constant of 0.15 N/m at a resonance frequency of 13 kHz. All images were recorded under ambient air conditions at room temperature (25°C ±1). The surface morphology of yttrium titanate film was examined using high-resolution scanning electron microscopy (SEM) with an energy dispersive spectroscopic (EDS) microanalysis system. The SEM analysis was performed using a Quanta FEG

250 instrument with a field emission gun from FEI Company in the Netherlands. In contact angle method, water droplets were deposited on the surfaces of the thin films. The contact angle measurements were performed using a Shape Analysis System model DSA258 instrument from KRUSS GmbH. The drop images were captured over time using a video camera, and an image analysis was conducted to determine the contact angle.

3. Results and Discussion

3.1 Characterization of $Y_2Ti_2O_7$ coated Steel

3.1.1. X-ray diffraction (XRD)

The X-ray diffraction patterns presented in **Figure 1a-b** show the evolution of the $Y_2Ti_2O_7$ phase on the coated steel at different calcination temperatures. **Figure 1a** demonstrates the emergence of the $Y_2Ti_2O_7$ phase, while **Figure 1b** displays the substrate peaks. The dominance of substrate peaks in XRD patterns at different calcination temperature can be attributed to the porous nature of the coatings (Nagarajan and Rajendran, 2009). The crystal data of the prepared $Y_2Ti_2O_7$-coated steel are listed in **Table 1**.

Table 1. XRD analysis of the prepared $Y_2Ti_2O_7$ coated steel substrate at different calcination temperatures.

Cal. Temp. (°C)	2θ (degree)	FWHM	Crystal size (nm.)	Lattice parameter (A°)
700	30.7	0.6298	13.7	10.07832
800	30.6	0.1920	44.8	10.11489
900	30.4	0.1968	43.7	10.17399

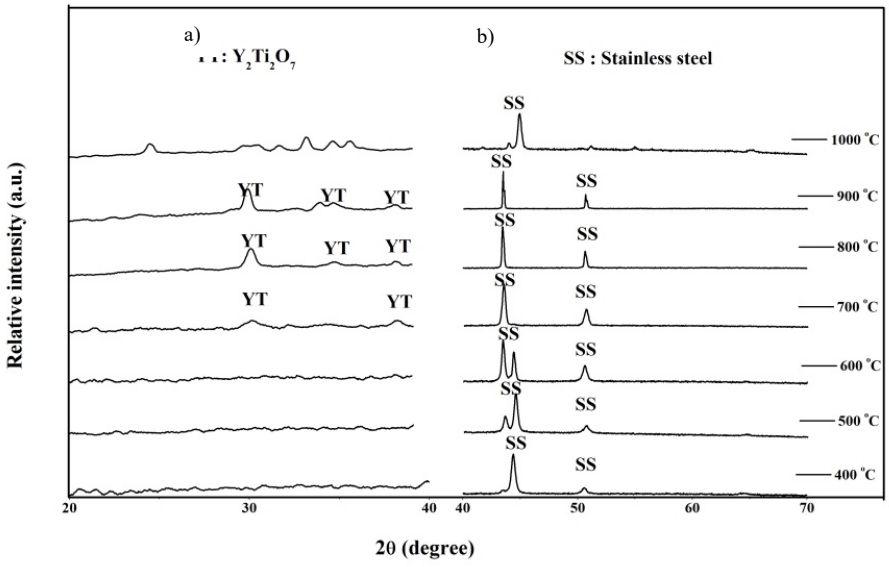

Figure 1. XRD pattern of $Y_2Ti_2O_7$ coated steel substrate at different calcination temperatures.

At calcination temperatures of 400, 500 and 600 °C, only steel substrate pattern was dominated with phase transformation (Mumtaz *et al.*, 2003, Yang *et al.*, 2008, Chen *et al.*, 2007). When the calcination temperature increased to 700 °C, characteristic $Y_2Ti_2O_7$ reflection peaks

appeared at 2θ = 30.7° (PDF#89- 2065), in addition to the steel peaks (Lavanya *et al.*, 2021, Yu *et al.*, 2022, Yu *et al.*, 2021). The main peak of $Y_2Ti_2O_7$ shifted to a lower angle as the calcination temperature increased from 700 to 900 °C. The crystal size values of $Y_2Ti_2O_7$ on the surface of the coated steel samples, calcinated at 700, 800, and 900 °C, were calculated using the Scherrer formula (Saif *et al.*, 2015) to be 13.7, 44.8, and 43.7 nm, respectively. Additionally, the maximum full width at half maximum (FWHM) values for $Y_2Ti_2O_7$-coated steel samples decreased as calcination temperature increased (**Table 1**). This suggests that calcination treatment significantly influences the crystallinity of $Y_2Ti_2O_7$ (Chen *et al.*, 2011b). Moreover, the lattice parameter slightly increased as a function of calcination temperature (Chen *et al.*, 2011b, Nagarajan and Rajendran, 2009) (**Table 1**). These results indicate that the formation and crystallization of the $Y_2Ti_2O_7$ phase on the steel surface commence at an annealing temperature of 700 °C (**Figure 1**).

3.1.2 Atomic Force Microscopy (AFM)

The surface topography of the steel under different experimental conditions was studied using AFM technique. **Figure 2** displays the 2D and 3D AFM images for both uncoated and $Y_2Ti_2O_7$-coated steel substrate calcinated at 900 °C before and after exposure to 1.0 M HCl as a corrosive medium for 24 hours. The surface roughness parameters, including mean roughness (R_a) and root mean square roughness (R_{rms}) (Nagarajan and Rajendran, 2009) were calculated and are shown in **Figure 2**.

The uncoated steel surface exhibited a few scratches with low roughness values (R_a = 2.9 nm, R_{rms} = 2.2 nm) due to the polishing treatment (**Figure 2a-b**). However, after exposure to the corrosive medium, the steel surface became rough with numerous bumps and cavities (**Figure 2c-d**). The roughness parameters of steel surface after exposure to 1.0 M HCl were measured as R_a = 18.8 nm and R_{rms} = 22.7 nm which are higher than those of uncoated steel (Abdelshafi *et al.*, 2022a). On the other hand, the AFM images of the $Y_2Ti_2O_7$-coated steel substrate before and after exposure to 1.0 M HCl revealed a uniform and homogeneous distribution of the smoothed $Y_2Ti_2O_7$ film on steel surface (**Figure 2f-i**). The roughness parameters of the $Y_2Ti_2O_7$-coated steel substrate were higher than those of the uncoated steel (Abdullahi *et al.*, 2021) (Ra =10.7 nm and R_{rms} = 13.2 nm). This can be attributed to the adhesion and growth of the $Y_2Ti_2O_7$ film on the surface. A slight decrease in the roughness parameter of the $Y_2Ti_2O_7$-coated steel substrate was observed after exposing the $Y_2Ti_2O_7$ film to the corrosive medium (Ra = 9.4 nm and R_{rms} = 11.7 nm). The low roughness parameter of the HCl-treated $Y_2Ti_2O_7$-coated steel substrate, compared to the HCl-treated uncoated steel, indicates that the surface was protected. This confirms that the $Y_2Ti_2O_7$ coating acts as an efficient barrier, protecting the steel surface from corrosion.

3.1.3 Scanning Electron Microscopy (SEM)

Figure 3 illustrates low-resolution and high-resolution SEM images of both uncoated and $Y_2Ti_2O_7$-coated steel substrate calcinated at 900 °C, before and after exposure to 1.0 M HCl for 24 hours as a corrosive medium. Prior to the corrosion test, the steel surface exhibited a few small pits (**Figure 3a-b**). However, after immersion in the corrosive medium, extensive corrosion in the form of shallow micro-pits was observed (**Figure 3c-d**). In contrast, the coated steel surface displayed a uniform distribution of $Y_2Ti_2O_7$ grains, forming a smooth, porous, and dense coating on the steel surface (**Figure 3e-f**).

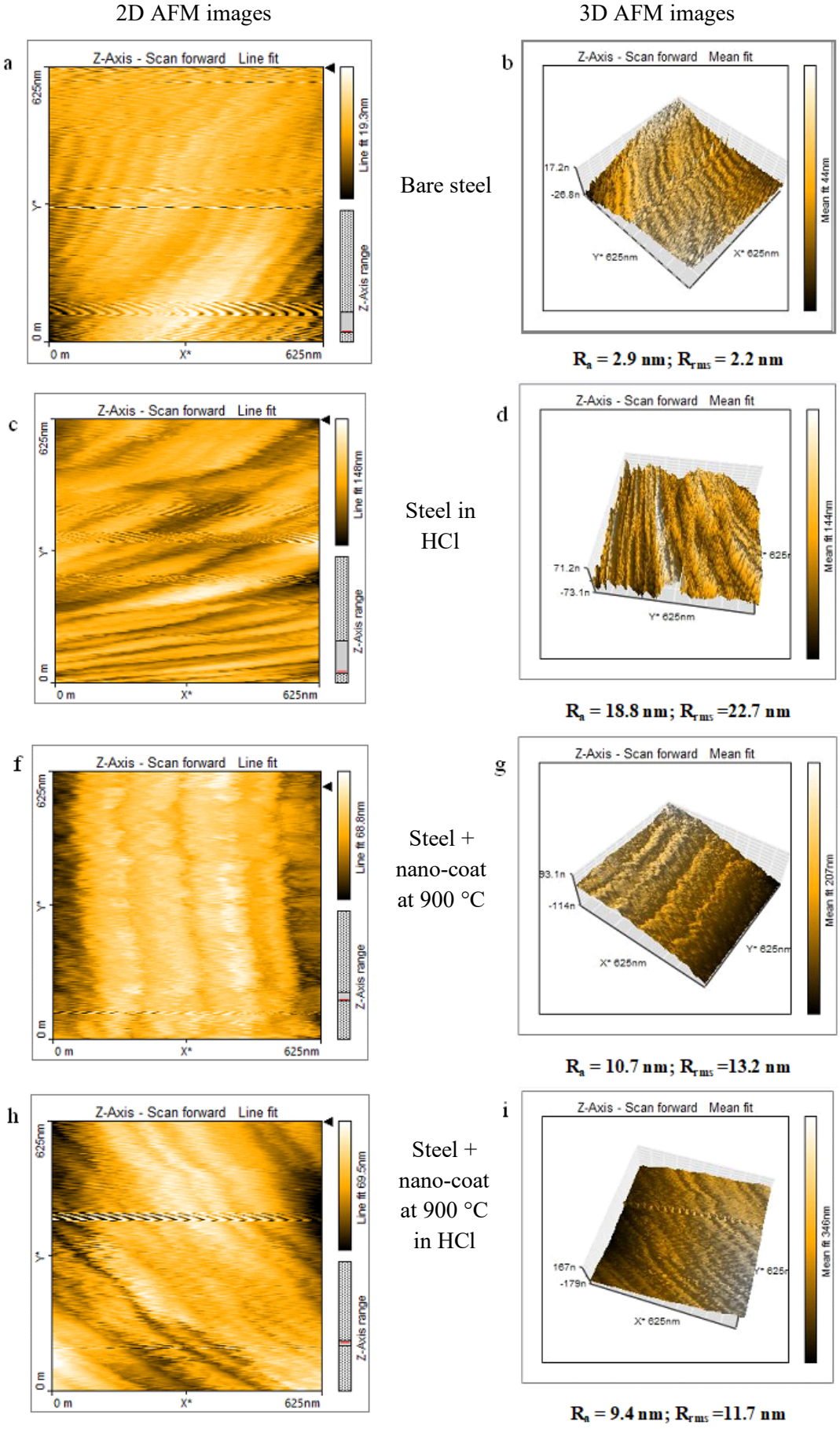

Figure 2. AFM images of uncoated steel and $Y_2Ti_2O_7$-coated steel substrate calcinated at 900°C before and after exposure to 1.0 M HCl as a corrosive medium.

The $Y_2Ti_2O_7$ grains had a small average size of 35 nm. Interestingly, the same morphological structure and grain size of the $Y_2Ti_2O_7$ thin film were maintained after immersion in the corrosive medium (1.0 M HCl for 24h). No noticeable cracking, pits, or open grain boundaries were observed on the $Y_2Ti_2O_7$ thin film after exposure to the corrosive medium (**Figure 3g-h**). The uniform distribution of small grains contributed to the formation of a compact and dense thin film, which effectively prevented corrosive species from reaching the interface between the $Y_2Ti_2O_7$ thin film and substrate. This unique thin film structure enhanced the corrosion protection properties of the coating.

EDS analysis was conducted to determine the surface elemental composition (**Figure 4a-c**). The EDS spectrum of uncoated steel has characteristic peaks corresponding to the elemental composition of steel (Fe, Cr, Mn, Ni) (**Figure 4a**). The EDS results of the $Y_2Ti_2O_7$-coated steel substrate (**Figure 4b**) confirmed the presence of titanium, yttrium and oxygen in addition to steel elements. A significant decrease in the atomic percentages of steel elements was observed after coating with $Y_2Ti_2O_7$, indicating the presence of $Y_2Ti_2O_7$ on the steel surface and the preparation of a highly pure coating. No changes were observed in the elemental composition and atomic percentages of the $Y_2Ti_2O_7$-coated steel surface before and after exposure to 1.0 M HCl (**Figure 4b-c**). This observation was further supported by EDS elemental mapping analysis (**Figure 5a-b**), which revealed a uniform distribution of coat elements on the steel substrate before and after exposure to the corrosive medium.

3.2 Hydrophobicity character of the $Y_2Ti_2O_7$ coated steel substrate

To assess the impact of the $Y_2Ti_2O_7$ thin film on the hydrophobicity of the steel substrate under different experimental conditions, a contact angle (CA) measurements were conducted using the sessile drop technique (John *et al.*, 2019). **Figure 6** presents photographs illustrating the water contact angles of the steel substrate coated with $Y_2Ti_2O_7$ at various calcination temperatures, showing higher angles compared to the uncoated substrate. Furthermore, no significant difference was observed in the contact angle of the coated steel substrate before and after immersion in the corrosive medium (1.0 M HCl for 24 hours) (**Figure 6**). These findings indicate an improvement in the hydrophobic nature of the steel substrate in the presence of the $Y_2Ti_2O_7$ thin film. The hydrophobic character of the thin film plays a crucial role in impeding the diffusion and interaction of corrosive molecules and ions (H_2O, O_2, Cl^-) with the steel substrate (Nazeer and Madkour, 2018). Therefore, the $Y_2Ti_2O_7$ thin film enhances the hydrophobic properties of the steel substrate, which is vital for protecting it from corrosion.

3.3 Electrochemical measurements

3.3.1 Electrochemical frequency modulation measurements

Electrochemical frequency modulation (EFM) is an AC electrochemical technique widely used for corrosion studies and evaluating the efficacy of protective coatings. It provides valuable insights into the electrochemical behavior of materials, including corrosion rate, coating impedance, and capacitance. EFM involves applying a small-amplitude alternating voltage perturbation to the working electrode at various frequencies while monitoring the resulting current response. This non-destructive and real-time approach enables the investigation of corrosion protection properties and the assessment of coating performance in different environments (Ali *et al.*, 2019, Abdel-Rehim *et al.*, 2006).

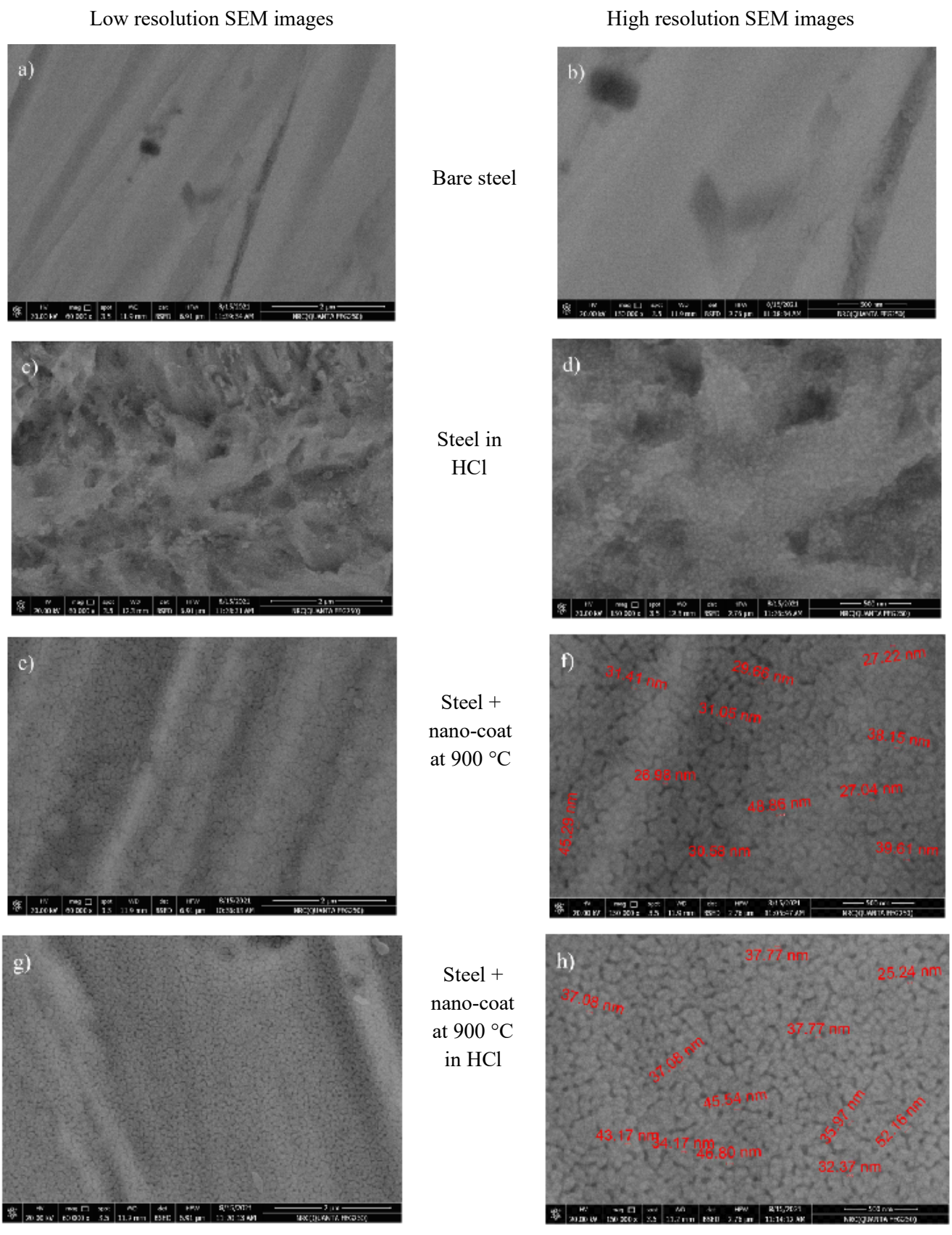

Figure 3. SEM images for of uncoated steel and $Y_2Ti_2O_7$-coated steel substrate calcinated at 900°C before and after exposure to 1.0 M HCl as a corrosive medium.

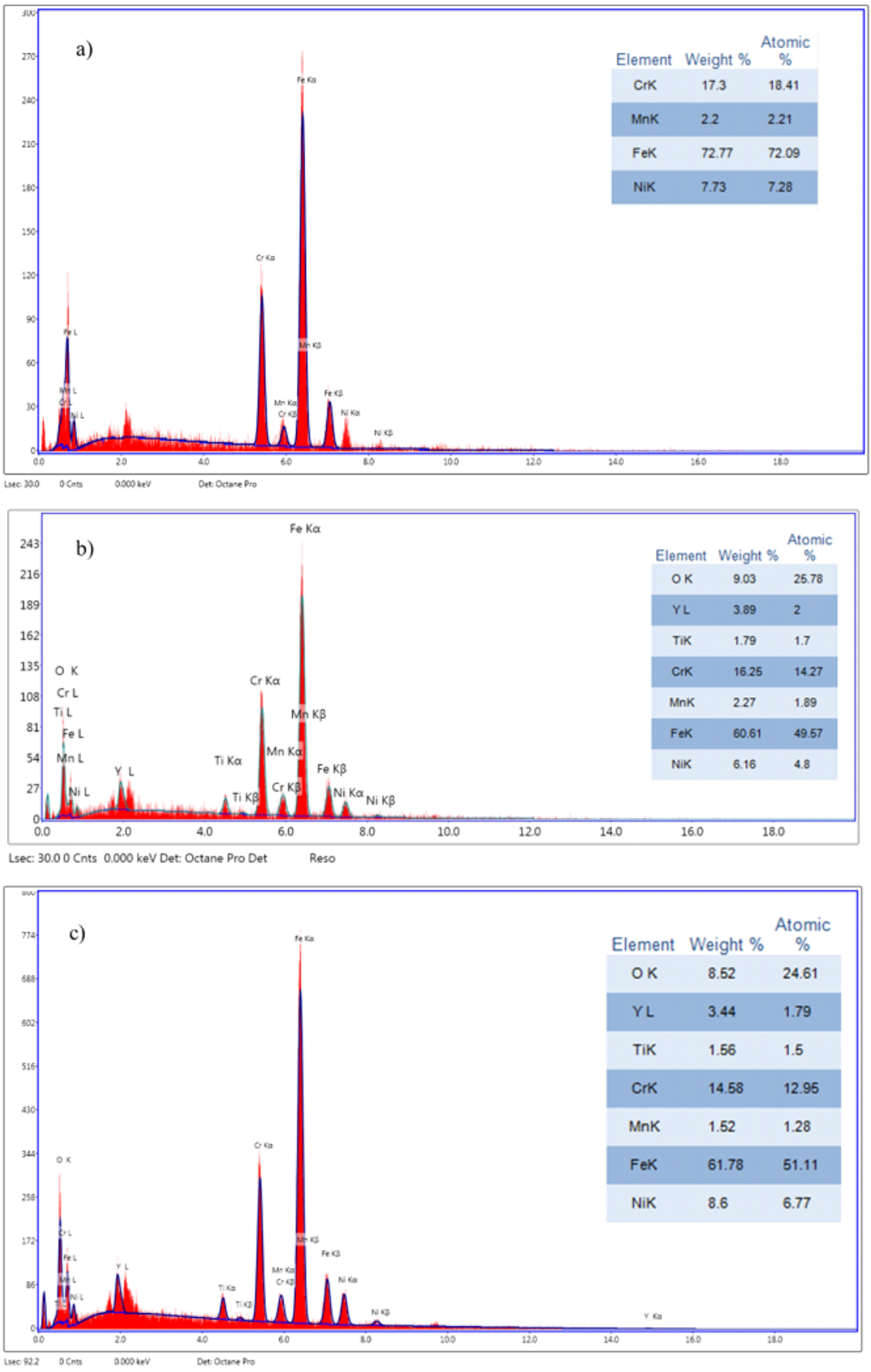

Figure 4. EDS spectra of uncoated steel (a), $Y_2Ti_2O_7$ coated steel substrate calcinated at 900°C before (b) and after (c) exposure to 1.0 M HCl.

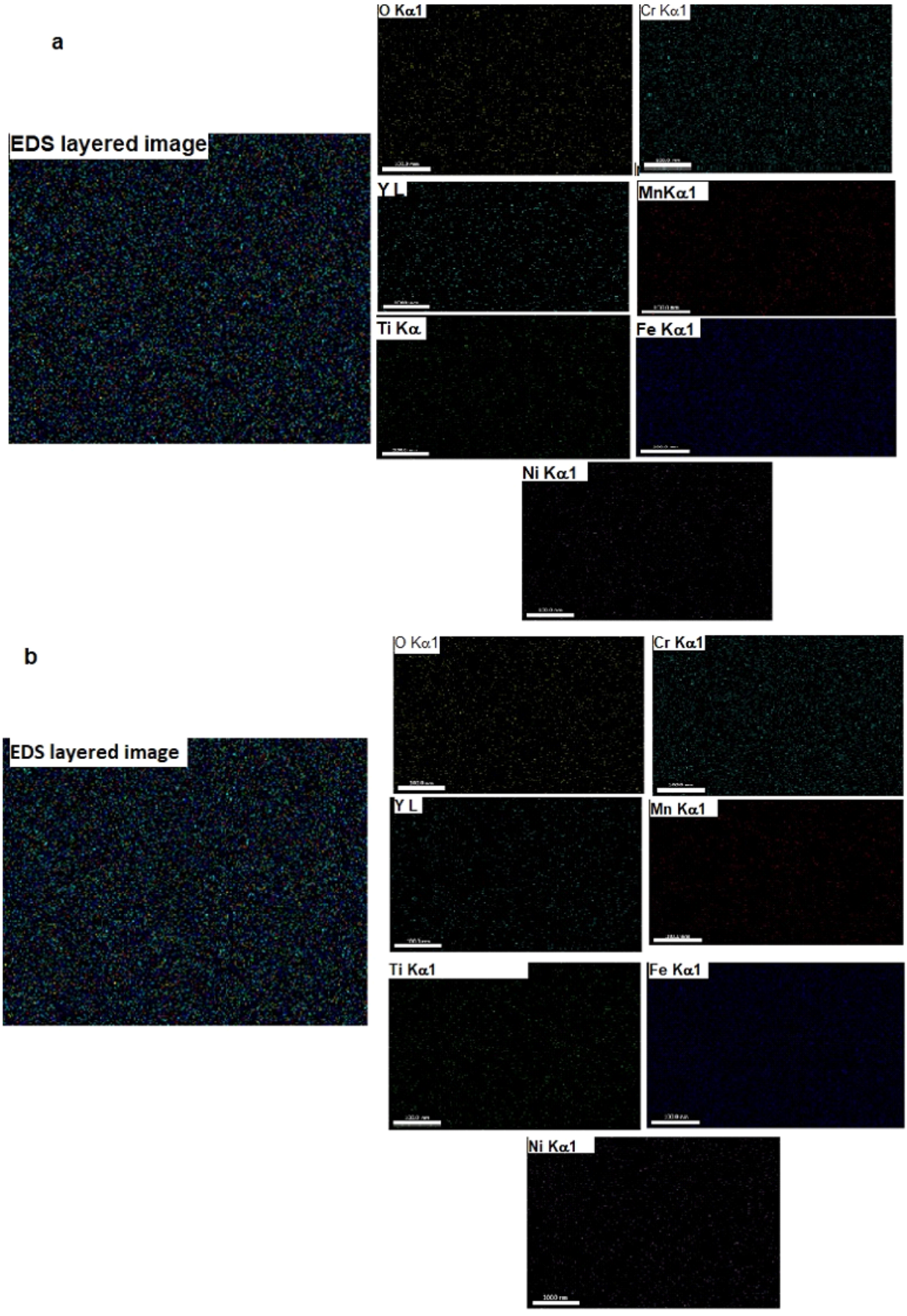

Figure 5. EDS elemental mapping of $Y_2Ti_2O_7$-coated steel substrate before (a) and after (b) exposure to 1.0 M HCl

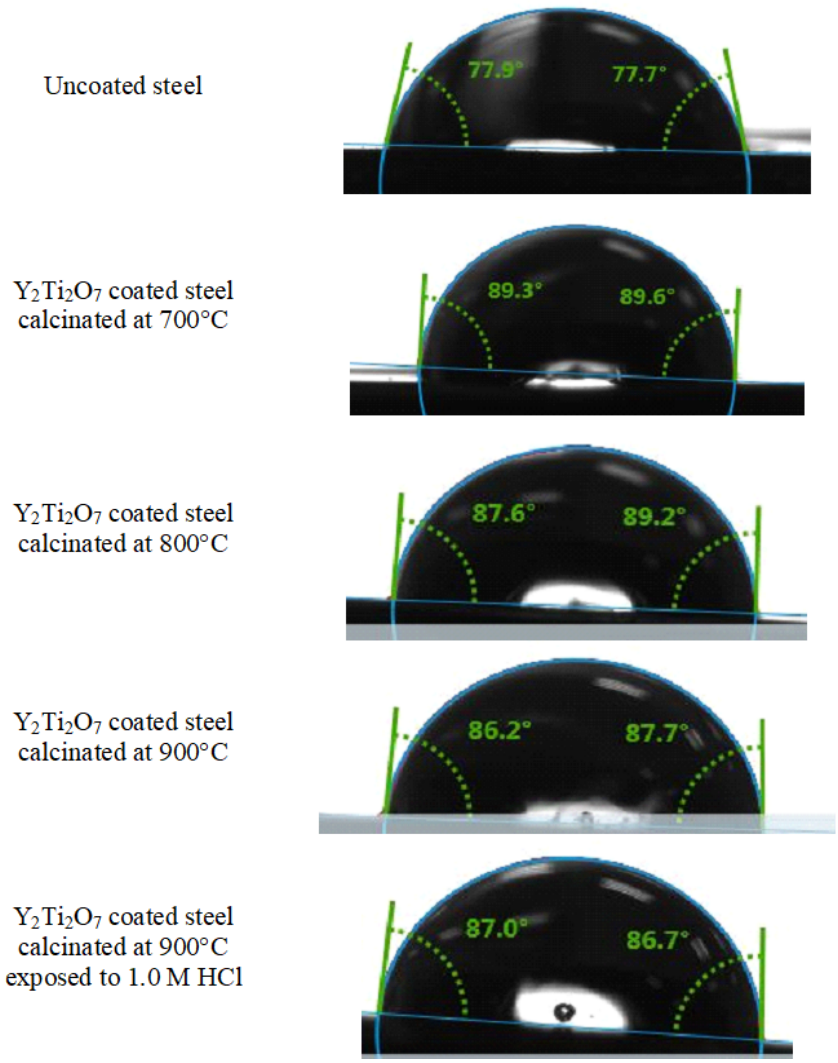

Figure 6. The static contact angle photographs of uncoated and $Y_2Ti_2O_7$ coated steel at different calcination temperatures.

The electrochemical parameters, including corrosion current density (i_{corr}), Tafel constants (β_a and β_c), the causality factors (CF-2 and CF-3) and corrosion rate (CR), were calculated using the EFM140 application of the Gamry 3000 instrument through the equations listed below. These parameters, along with the coating's inhibition efficiency η_{EFM} % are listed in **Table 2**.

$$i_{corr} = \frac{\left(i_{\omega_1 \cdot \omega_2}\right)^2}{2\sqrt{8 i_{\omega_1 \cdot \omega_2} i_{2\omega_2 \pm \omega_1} - 3\left(i_{\omega_1 \cdot \omega_2}\right)^2}}$$

$$\beta_a = \frac{i_{\omega_1 \cdot \omega_2} U}{i_{\omega_2 \pm \omega_1} + \sqrt{8 i_{\omega_1 \cdot \omega_2} i_{2\omega_2 \pm \omega_1} - 3\left(i_{\omega_1 \cdot \omega_2}\right)^2}}$$

$$\beta_c = \frac{i_{\omega_1 \cdot \omega_2} U}{-i_{\omega_2 \pm \omega_1} + \sqrt{8 i_{\omega_1 \cdot \omega_2} i_{2\omega_2 \pm \omega_1} - 3\left(i_{\omega_1 \cdot \omega_2}\right)^2}}$$

$$\text{Causality factor 2 (CF - 2)} = \frac{i_{\omega_1 \pm \omega_2}}{i_{2\omega_1}} = 2$$

$$\text{Causality factor 3 (CF - 3)} = \frac{i_{2\omega_1 \pm \omega_2}}{i_{3\omega_1}} = 3$$

$$CR_{mpy} = 0.13 i_{corr} (e/\rho)$$

where i_{corr} is corrosion current density, where ω_2 and ω_1 denote the applied frequencies {$\omega_2 > \omega_1$; ($\omega = 2\pi f$)}, and U represents the amplitude of the sine wave perturbation, $i_{2\omega_1}$ is the measured harmonic components, correspond to angular frequencies of $2\omega_1$. Similarly, $i_{3\omega_1}$ is the measured harmonic components, correspond to angular frequencies of $3\omega_1$. Additionally, the intermodulation

components, $i_{\omega_1 \pm \omega_2}$, $i_{2\omega_2 \pm \omega_1}$, and $i_{2\omega_1 \pm \omega_2}$, represent current responses measured at angular frequencies $\omega_1 \pm \omega_2$, $2\omega_2 \pm \omega_1$ and $2\omega_1 \pm \omega_2$, respectively. CR_{mpy} is the corrosion rate (mils/year), (e) is the equivalent weight of the metal and (ρ) is the density of the metal.

Table 2. Electrochemical kinetic parameters obtained by EFM technique for uncoated 304 stainless steel and coated samples with yttrium titanate calcinated at different temperature in 1.0 M HCl at 25°C ±1.

Cal. Temp. (°C)	i_{corr} (μA.cm^{-2})	β_a (mV/dec)	β_c (mV/dec)	CR (mpy)	CF-2	CF-3	η_{EFM} %
Blank	461.10	92.94	115.50	210.70	1.67	1.68	-------
400	153.20	78.04	155.10	70.00	1.75	2.28	66.78
500	488.00	59.90	84.98	223.00	1.29	2.57	-------
600	579.90	85.59	254.70	265.00	1.91	1.82	-------
700	12.45	54.30	74.70	5.69	1.95	2.28	97.29
800	3.23	84.52	133.30	1.48	1.90	1.48	99.30
900	1.38	80.32	172.50	630.60	1.83	1.83	99.70
1000	50.81	55.16	73.79	23.22	1.24	1.44	88.98

The intermodulation spectra presented in **Figure 7** and **Table 2** show a decrease in corrosion current density at 400 °C compared to the blank sample, with an inhibition efficiency of 66.78%. This behavior can be attributed to the initiation of a protective layer (mainly consisting of Y_2O_3, TiO_2 and Cr_2O_3) on the steel surface due to phase changes in the steel at 400 °C. This protective layer acts as a barrier against the corrosion process, leading to a decrease in corrosion current density (i_{corr}= 153.20 μA.cm^{-2}). However, at higher calcination temperatures (500 and 600 °C), the steel surface may undergo phase transformations or structural changes (as indicated by the XRD pattern in **Figure 1**), which can affect its protective properties. For instance, the coating may become more porous or develop cracks, allowing hydrochloric acid to reach the underlying steel surface. This results in an increase in the corrosion current density, from i_{corr} = 488.00 μA.cm^{-2} at 500 °C to i_{corr} =579.90 μA.cm^{-2} at 600 °C, accompanied by a significant reduction in the inhibition efficiencies of -5.83% and -25.76%, respectively. These negative values of η_{EFM} % only indicate corrosion acceleration and are therefore omitted from the table.

At higher temperatures (700, 800, and 900 °C), the XRD pattern reveals the formation of a yttrium titanate coating, which improves the protective properties of the steel. The coating may become denser or develop a more uniform microstructure, acting as a barrier against the corrosion process and resulting in a decrease in the corrosion current density. In summary, the corrosion resistance of the steel coated with yttrium titanate is significantly influenced by the calcination temperature and the resulting microstructure and composition of the coating. Yttrium titanate exhibits enhanced protection when calcinated at temperatures of 700, 800, and 900 °C (inhibition efficiencies of 97.29%, 99.30%, and 99.70%, respectively), as evidenced by the decrease in corrosion current density (i_{corr} = 12.45, 3.23, and 1.38 μA.cm^{-2}, respectively). These results are consistent with the XRD analysis in **Figure 1**. However, the decline in corrosion resistance after 900 °C can be attributed to several factors. At such high temperatures, the yttrium titanate coating may undergo decomposition or react with the underlying steel substrate, compromising its protective properties. This could result in the formation of a layer of yttrium oxide (Y_2O_3) on the coating surface, which may not be as effective at preventing steel corrosion as the original yttrium titanate layer.

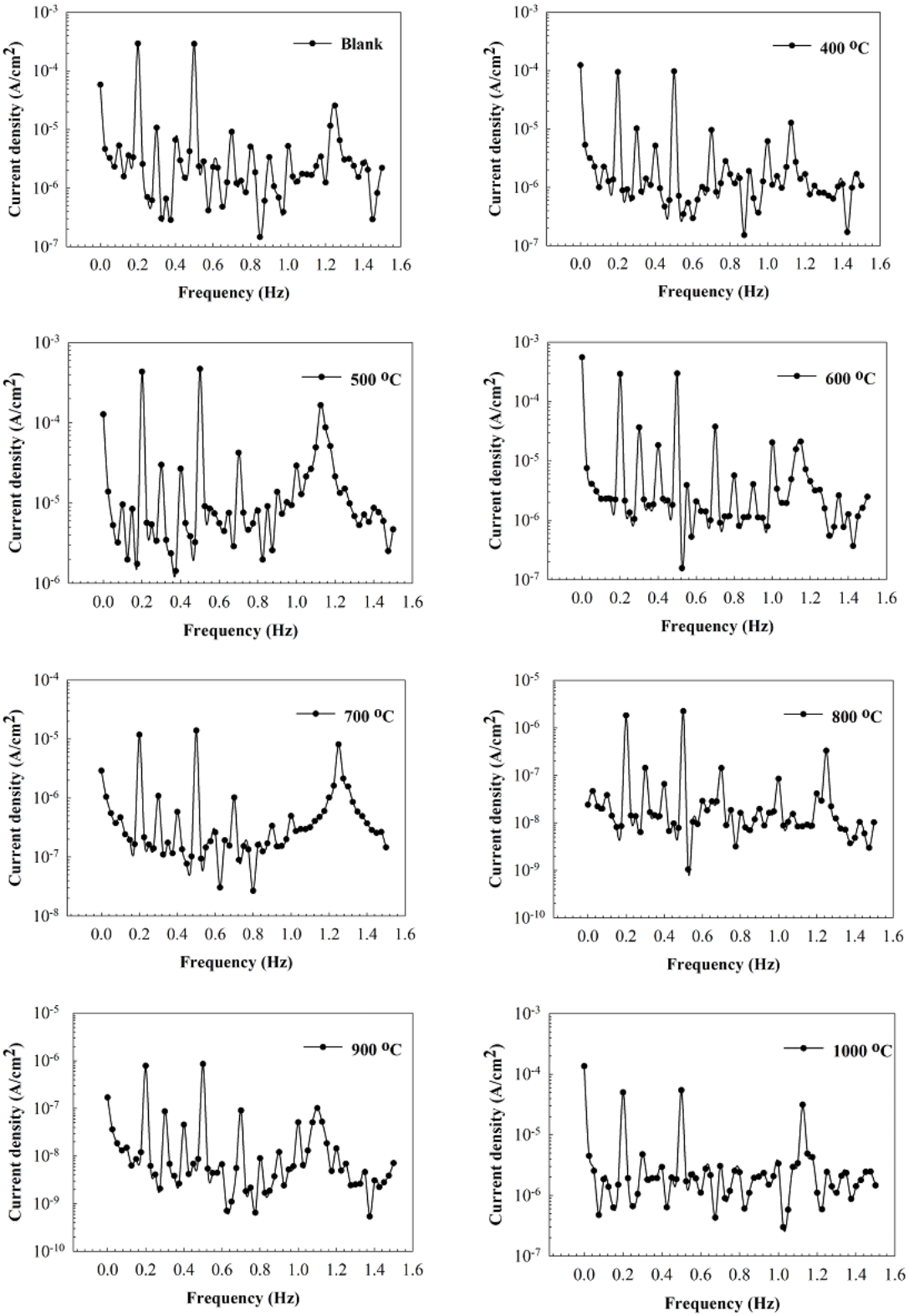

Figure 7. Intermodulation spectra for uncoated 304 stainless steel and coated samples with yttrium titanate calcinated at different temperature (400, 500, 600, 700, 800, 900 and 1000 °C) in 1.0 M HCl at 25 °C±1.

Additionally, exposure to high temperatures can lead to the formation of defects or cracks in the coating, allowing the corrosive environment to penetrate the underlying steel surface and increase the corrosion current density. Moreover, the formation of specific crystal phases of yttrium titanate at

higher temperatures may reduce its chemical stability and protective ability. Therefore, while the behavior of the yttrium titanate coating at high temperatures is complex and can enhance corrosion resistance in certain cases, it is crucial to thoroughly investigate the underlying mechanisms involved to ensure its effectiveness as a protective layer.

3.3.2 Electrochemical impedance spectroscopy measurements

In this study, the corrosion inhibition properties of a yttrium titanate coating on steel surfaces immersed in 1.0 M HCl solutions were evaluated and compared with those of uncoated surface. The corrosion mechanism in 1.0 M HCl solutions typically involves the dissolution of iron ions from the steel surface and the formation of iron chloride compounds. The corrosion rate can be controlled by the formation of a protective oxide layer on the surface or by the application of a protective coating. We investigated the effect of calcination temperature on the protective performance of yttrium titanate coating electrochemical impedance spectroscopy using (EIS).

The Nyquist (**Figure 8**) and Bode (**Figure 10**) plots obtained from the impedance data exhibited different behaviors at varying calcination temperatures. At 400°C, the polarization resistance (R_p) of the coating was higher than that of the blank, indicating better inhibition efficiency. However, at 500 and 600°C, the Nyquist plots showed lower polarization resistance compared to the blank, suggesting a lower inhibition efficiency of -20.01% and -36.54%, respectively. These negative values of inhibition efficiency indicate corrosion acceleration and are omitted from the table. At higher temperatures (700-900°C), the formation of yttrium titanate coating increased the polarization resistance and hence the inhibition efficiency, as indicated by the higher R_p values in the Nyquist plots. The analysis of the equivalent circuit (**Figure 9**) revealed that the protective performance of the coating was related to the formation of a compact and homogeneous yttrium titanate layer on the surface, which effectively blocked the diffusion of H^+ ions and reduced the corrosion rate. However, above 900°C, the inhibition efficiency decreased, as shown by the lower R_p values in the Nyquist plots. This decrease could be attributed to the formation of cracks and defects in the coating, exposing the underlying steel surface to the corrosive environment (HCl) and promoting the corrosion rate.

The results highlight the critical role of the calcination temperature in determining the protective performance of the yttrium titanate coating and emphasize the need for careful optimization of the coating process parameters to achieve the desired inhibition efficiency.

The proposed equivalent circuit used to describe the studied system consists of solution resistance (R_s), a resistor (R_p) in parallel with a constant phase element (CPE), and a resistor (R_L) in parallel with an inductor (L). The Nyquist plot displays a semicircle and an inductive loop, where the semicircle represents the charge transfer resistance and double layer capacitance of the coating, while the inductive loop indicates the presence of inductance in the coating. The electrochemical parameters obtained from EIS, such as R_s, CPE with its heterogeneity (n), R_p, and L with its resistance (R_L), were calculated by fitting the impedance spectra to the equivalent circuit model shown in **Figure 9** and presented in **Table 3**.

The analysis of the equivalent circuit revealed that the polarization resistance (R_p) of the steel electrode increased at 400°C (R_p =0.463 kΩ.Cm^2) and then sharply decreased between 500 and 600°C. As the calcination temperature increased from 700 to 900°C, the polarization resistance sharply increased, reaching its maximum at 900°C (R_p = 44.40 kΩ.Cm^2), along with an inhibition efficiency of 99.6%. At a calcination temperature of 1000°C, the polarization resistance decreased (R_p= 1.27 kΩ.Cm^2), accompanied by an inhibition efficiency of 86.0%.

The presence of inductive loops in Nyquist plots and the use of constant phase elements in equivalent circuits are common when describing the studied system. The inductive loop represents physical inductance in the system, while the constant phase element represents non-ideal behavior. The inductive loop can influence EIS data by contributing to the low-frequency response, resulting in an increase in impedance magnitude with increasing frequency. The constant phase element can also affect EIS data by representing non-ideal behavior, often observed as a depressed semicircular arc in the Nyquist plot, indicating a more complex electrochemical process. Unlike a pure capacitor or resistor, the CPE does not maintain a constant phase angle over a wide range of frequencies. Instead, it exhibits a power law frequency dependence, which can lead to a depressed semicircular arc in the Nyquist plot

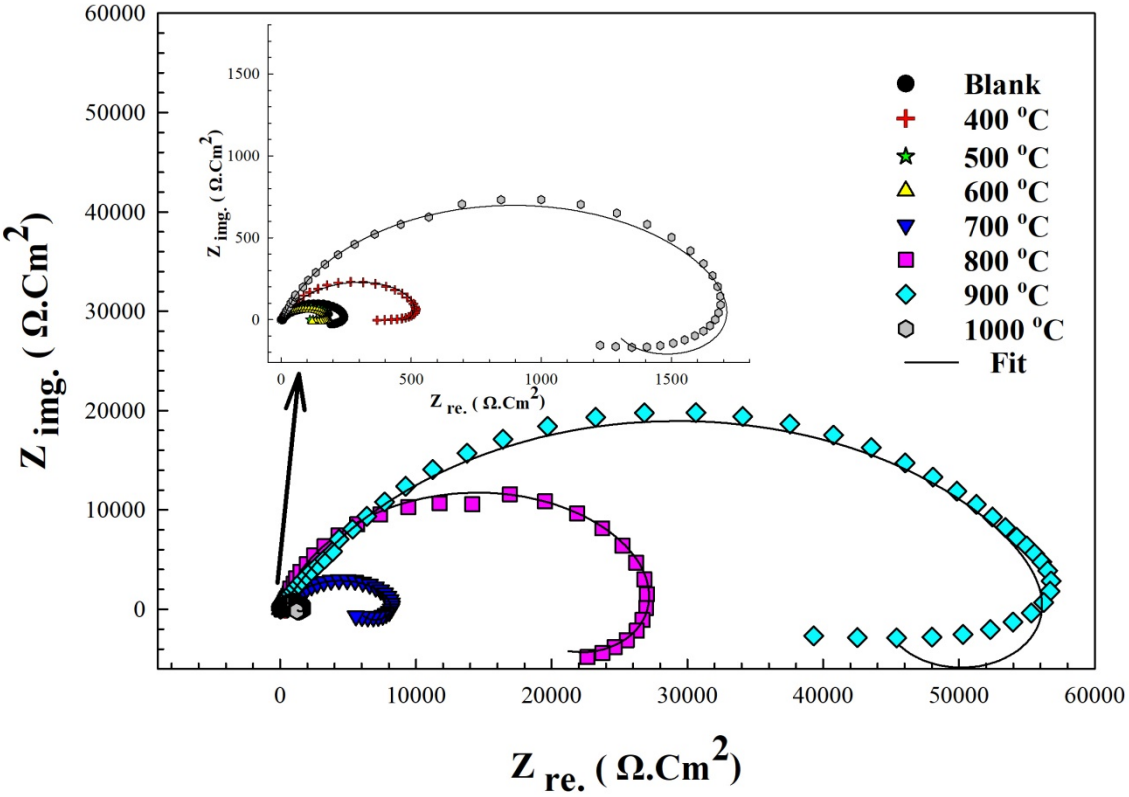

Figure 8. Nyquist plots uncoated 304 stainless steel and coated samples with yttrium titanate calcinated at different temperature in 1.0 M HCl at 25°C ±1.

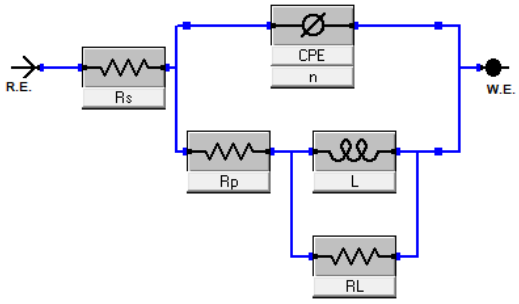

Figure 9. Equivalent circuit used to model impedance data for uncoated 304 stainless steel and coated samples with yttrium titanate calcinated at different temperature in 1.0 M HCl at 25°C ±1.

Table 3. Electrochemical kinetic parameters obtained by EIS technique for for uncoated 304 stainless steel and coated samples with yttrium titanate calcinated at different temperature in 1.0 M HCl at 25°C ±1.

Cal. Temp. (°C)	R_s ($\Omega.Cm^2$)	R_L ($k\Omega.Cm^2$)	R_p ($k\Omega.Cm^2$)	CPE ($d\Omega^{-1}.cm^{-2}.S^n$)	n x 10^{-1}	L ($kH.cm^2$)	η_{EIS} %
Blank	6.527	0.066	0.178	19.400	8.470	0.152	-----
400	1.438	0.198	0.463	26.000	7.960	0.067	61.688
500	1.356	0.109	0.148	113.000	7.050	0.051	------
600	0.694	0.072	0.130	68.400	7.000	0.155	------
700	20.390	3.040	5.920	1.880	7.320	7.630	96.999
800	109.300	11.500	17.800	1.230	8.640	56.700	99.000
900	77.630	14.100	44.400	0.098	7.330	36.700	99.599
1000	6.116	0.515	1.270	4.180	8.470	1.080	86.002

3.3.3 Tafel polarization measurements

Table 4 presents the electrochemical parameters extracted from **Figure 11**, which includes corrosion current densities (i_{corr}), corrosion potential (E_{corr}), anodic Tafel slope (β_a), cathodic Tafel slope (β_c) and, corrosion rate (CR).

Table 4. Electrochemical kinetic parameters obtained by Tafel polarization technique for blank and coated steel in1.0 M HCl at 25 ± 1 °C at various calcination temperatures.

Cal. Temp. (°C)	i_{corr} ($\mu A.cm^{-2}$)	$-E_{corr}$ (mV Vs. SCE)	βa (mV/dec.)	βc (mV/dec.)	CR (mpy)	η_{Tafel} %
Blank	571.0	428.0	84.2	88	260	-------
400	233.0	424.0	86.6	112.2	106.4	59.19
500	708.0	427.0	156.0	109.8	323.3	-------
600	874.0	428.0	222.3	120.4	399.2	-------
700	18.2	421.0	83.1	105.0	8.314	96.81
800	4.84	365.0	86.00	156.4	2.213	99.15
900	1.98	379.0	48.6	99.3	0.9067	99.65
1000	86.6	423.0	184.1	91.7	39.56	84.83

In this study, we investigated the corrosion behavior of $Y_2Ti_2O_7$-coated steel calcinated at different temperatures in 1.0 M HCl. The experimental data showed that the corrosion current density initially decreased at 400 °C (i_{corr}= 233.0 $\mu A.cm^{-2}$) compared to the uncoated steel. This can be attributed to the formation of a passive film on the steel surface. However, at 500 and 600 °C, the corrosion current density increased (i_{corr}= 708.0 and 874.0 $\mu A.cm^{-2}$, respectively), indicating a higher rate of metal dissolution (CR= 323.3 and 399.2 mpy, respectively). The high CR was accompanied by negative values of inhibition efficiency (η_{Tafel} %) of -23.99% and -53.06%, respectively. These values were omitted from the table because there is no meaning to inhibition efficiency with negative sign. This corrosion acceleration may be due to the transformation of the steel phase at these temperatures, as observed in the XRD pattern. At 700, 800, and 900 °C, the corrosion current density sharply decreased (i_{corr}= 18.2, 4.84, and 1.98 $\mu A.cm^{-2}$, respectively), reaching maximum inhibition efficiency (η_{Tafel} % = 99.6%) at 900 °C. This can be attributed to the formation of a protective yttrium titanate phase on the steel surface. Above 900 °C, the corrosion current density increased again (i_{corr}= 86.6

μA.cm^{-2}), and the inhibition efficiency decreased (η_{Tafel} % = 84.83% at 1000 °C), potentially due to the degradation of the protective coating.

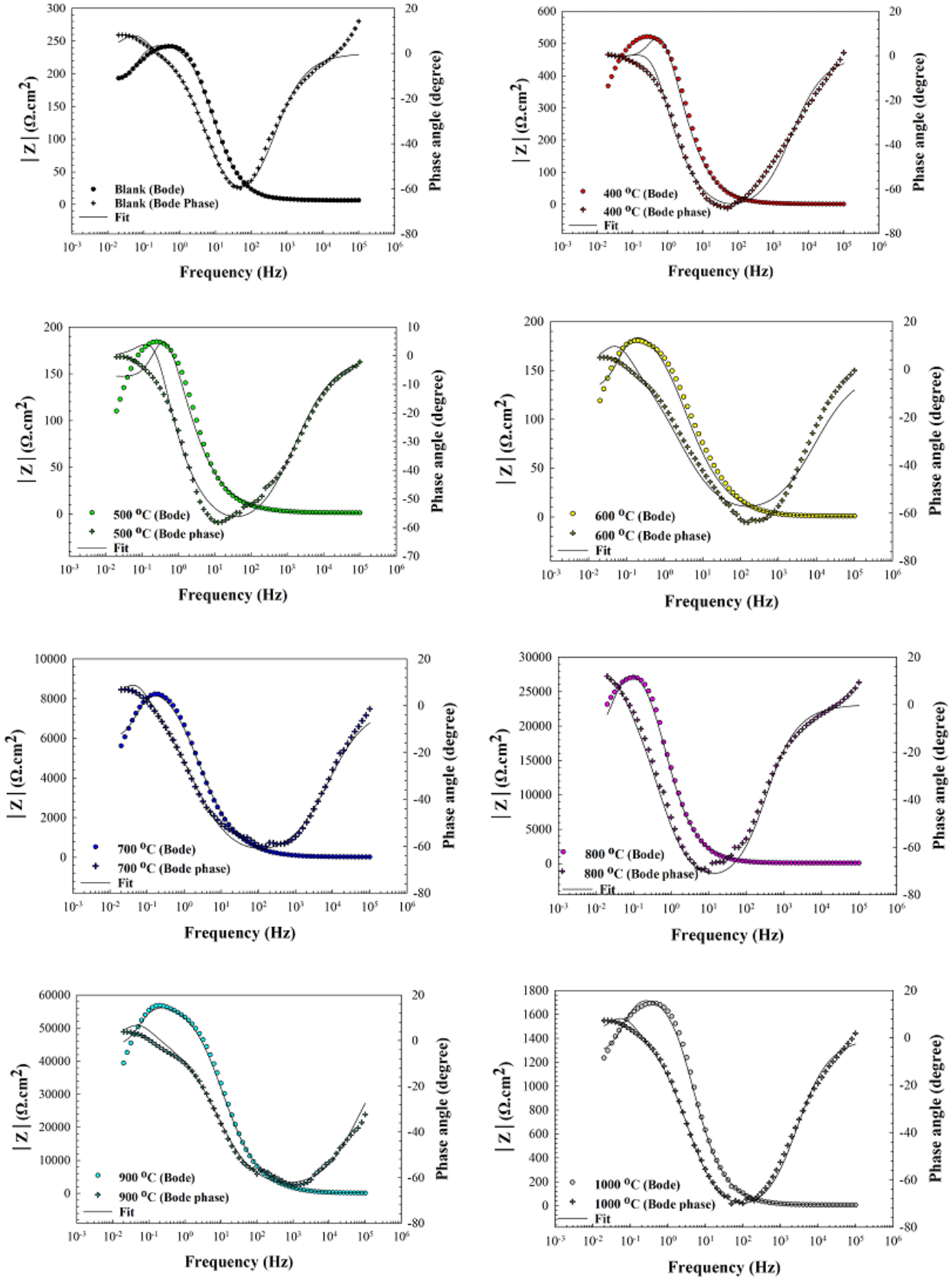

Figure 10. Bode plots for uncoated 304 stainless steel and coated samples with yttrium titanate calcinated at different temperature in 1.0 M HCl at 25°C ±1.

XRD analysis confirmed the formation of the yttrium titanate phase on the steel surface at 700, 800, and 900 °C, contributing to the decrease in corrosion current density. At 500 and 600 °C, the transformation of the steel phase may be responsible for the increase in corrosion current density.

On the other hand, the Tafel slopes remained nearly constant across the range of calcination temperatures, indicating a consistent anodic and cathodic reaction mechanism for the corrosion process. This information can be valuable for designing protective coatings that target specific reaction mechanisms.

In conclusion, the Tafel polarization technique is a valuable method for evaluating the corrosion behavior of steel in different environments and provides important insights into the effectiveness of corrosion inhibitors. The experimental data from this study emphasizes the significance of controlling the calcination temperature for the formation of protective coatings with enhanced corrosion resistance.

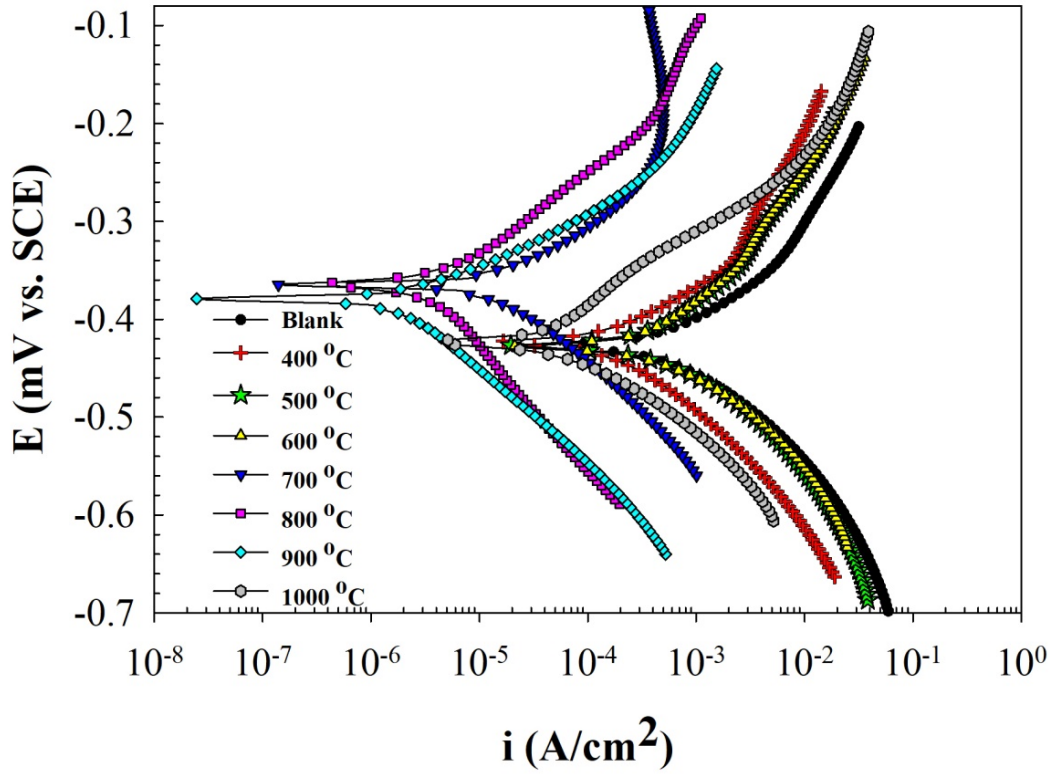

Figure 11. Anodic and cathodic Tafel polarization curves for blank and coated steel in1.0 M HCl at 25 ± 1 °C at various calcination temperatures.

Conclusion

A protective nano-yttrium titanate ($Y_2Ti_2O_7$) coating was developed for 304 stainless steel under acidic conditions (1.0 M HCl). The $Y_2Ti_2O_7$ coating was synthesized using the spin coating sol-gel method and calcined at different temperatures (400, 500, 600, 700, 800, 900, 1000 °C) for 2 hours. The coated steel samples were characterized using various surface analysis techniques, including X-ray diffraction analysis (XRD), atomic force microscopy (AFM), scanning electron microscopy (SEM), and energy dispersive X-ray analysis (EDS). XRD analysis confirmed the formation of the $Y_2Ti_2O_7$ phase starting at 700 °C, which remained stable up to 900 °C with the highest intensity. AFM measurements showed that the HCl-treated $Y_2Ti_2O_7$-coated steel substrate calcined at 900 °C

had lower roughness parameters (R_a = 9.4 nm and R_{rms} = 11.7 nm) compared to the HCl-treated uncoated steel (R_a = 18.8 nm and R_{rms} = 22.7 nm), indicating improved surface protection. SEM images further supported these findings. The $Y_2Ti_2O_7$ thin film exhibited a homogeneous distribution of small grains, low roughness parameter, and hydrophobic properties.

Electrochemical techniques, including electrochemical frequency modulation (EFM), electrochemical impedance spectroscopy (EIS), and Tafel polarization (dc technique), were employed to evaluate the corrosion inhibition performance. All three techniques consistently demonstrated that increasing the calcination temperature and the presence of the $Y_2Ti_2O_7$ phase improved the inhibition efficiency against corrosion in 1.0 M HCl. The maximum inhibition efficiency of approximately 99.6% was achieved at 900 °C. The results obtained confirm that the $Y_2Ti_2O_7$ coating efficiently acts as a protective barrier, safeguarding the austenitic 304 stainless steel surface against corrosion especially under acidic condition.

Acknowledgement: The authors would like to express their gratitude to the National Research Center, Desert Research Center, Petroleum Research Institute in Cairo, and Environmental Studies and Research Institute at Menoufia University in Sadat City for providing the characterization equipment.

References

Abdel-Rehim S. S., Khaled K. F. Abd-Elshafi N. S., (2006) Electrochemical frequency modulation as a new technique for monitoring corrosion inhibition of iron in acid media by new thiourea derivative, *Electrochim. Acta,* 51(16), 3269-3277. https://doi.org/10.1016/j.electacta.2005.09.018

Abdelshafi N. S., Ibrahim M. A., Badran A.-S. Halim S. A., (2022a) Experimental and theoretical evaluation of a newly synthesized quinoline derivative as corrosion inhibitor for iron in 1.0 M hydrochloric acid solution*, J. Mol. Struct.,* 1250, 131750-131770. https://doi.org/10.1016/j.molstruc.2021.131750

Abdelshafi N. S., Sadik M. A., Shoeib M. A. Halim S. A., (2022b) Corrosion inhibition of aluminum in 1 M HCl by novel pyrimidine derivatives, EFM measurements, DFT calculations and MD simulation, *Arab. J. Chem.,* 15(1), 103459-103485. https://doi.org/10.1016/j.arabjc.2021.103459

Abdullahi S. A., Akoba R., Khamlich S., Halindintwali S., Nuru Z. Y. Maaza M., (2021) Hydrothermal surface treatment of 434-L stainless-steel for spectra solar absorber application, *Infrared Phys. Technol.,* 117, 103848-103859. https://doi.org/10.1016/j.infrared.2021.103848

Ali S. M., Emran K. M. Messali M., (2019) Improved protection performance of modified sol-gel coatings with pyridinium-based ionic liquid for cast iron corrosion in 0.5 M HCl solution, *Prog. Org. Coat.,* 130, 226-234. https://doi.org/10.1016/j.porgcoat.2019.02.002

Almashhdani H. Alsaadie K., (2018) Corrosion Protection of Carbon Steel in seawater by alumina nanoparticles with poly (acrylic acid) as charging agent, *Mor. J. Chem.,* 6(3). doi: 10.48317/IMIST.PRSM/morjchem-v6i3.6214

Aslam R., Mobin M., Zehra S. Aslam J., (2022) A comprehensive review of corrosion inhibitors employed to mitigate stainless steel corrosion in different environments, *J. Mol. Liq.,* 364, 119992-120037. https://doi.org/10.1016/j.molliq.2022.119992

Behnamian Y., Mostafaei A., Kohandehghan A., Amirkhiz B. S., Zahiri R., Zheng W., Guzonas D., Chmielus M., Chen W. Luo J. L., (2017) A comparative study on the oxidation of austenitic alloys 304 and 304-oxide dispersion strengthened steel in supercritical water at 650°C, *J. Supercrit. Fluids,* 119, 245-260. https://doi.org/10.1016/j.supflu.2016.10.002

Boukerche S., Himour A., Bououdina M., Bensouici F. Ouchenane S., (2019) Multilayered ZnO/TiO_2 nanostructures as efficient corrosion protection for stainless steel 304, *Mater. Res. Express.,* 6(5), 055052-055067. doi: 10.1088/2053-1591/ab042f

Buyuksagis A., Kara S. Aksut A. A., (2015) The effect of polypyrrole and nickel plus polypyrrole coatings on corrosion behaviour AISI 304 stainless steel, *Prot. Met. Phys. Chem. Surf.,* 51(1), 155-166. doi: 10.1134/S2070205115010025

Chen A. Y., Zhang J. B., Song H. W. Lu J., (2007) Thermal-induced inverse γ/α′ phase transformation in surface nanocrystallization layer of 304 stainless steel, *Surf. Coat. Technol.,* 201(16), 7462-7466. https://doi.org/10.1016/j.surfcoat.2007.02.018

Chen H. X., Ma X. H., Bo S. S. Chen J. B., (2011a) Preparation of Fe/Cr doped SiO_2 thin film on 304 stainless steel substrate originated from corrosion, *Corros. Eng. Sci. Technol.,* 46(4), 453-457. doi: 10.1179/147842209X12464471864736

Chen Z., Gong W., Chen T. Li S., (2011b) Synthesis and Charaterization of Pyrochlore-Type Yttrium Titanate Nanoparticles by a Modified Sol-Gel Method, *Bull. Mater. Sci.,* 34, 429-434. doi: 10.1007/s12034-011-0116-2

Curkovic L., Curkovic H. O., Salopek S., Renjo M. M. Segota S., (2013) Enhancement of corrosion protection of AISI 304 stainless steel by nanostructured sol-gel TiO_2 films, *Corros. Sci.,* 77, 176-184. doi: 10.1016/j.corsci.2013.07.045

D'Isanto F., Smeacetto F., Martin H.-P., Sedlák R., Lisnichuk M., Chrysanthou A. Salvo M., (2021) Development and characterisation of a $Y_2Ti_2O_7$-based glass-ceramic as a potential oxidation protective coating for titanium suboxide (TiO_x), *Ceram. Int.,* 47(14), 19774-19783. https://doi.org/10.1016/j.ceramint.2021.03.316

Di Maggio R., Fedrizzi L., Rossi S. Scardi P., (1996) Dry and wet corrosion behaviour of AISI 304 stainless steel coated by sol-gel ZrO_2□CeO_2 films, *Thin Solid Films,* 286(1), 127-135. https://doi.org/10.1016/S0040-6090(95)08515-7

El-Haddad M. N. Elattar K. M., (2013) Role of novel oxazocine derivative as corrosion inhibitor for 304 stainless steel in acidic chloride pickling solutions, *Res. Chem. Intermed.,* 39(7), 3135-3149. doi: 10.1007/s11164-012-0826-0

El Ouadi Y., Beladjila A., Bouyanzer A., Kabouche Z., Bendaif H., Youssfi F., Berrabah M., Touzani R., Chetouani A. Hammouti B., (2017) The Palm oil from seed of Phoenix dactylifera (Oil of both Deglet Nour and Kentichi) as a natural antioxidants and Environment-Friendly inhibitors on the Corrosion of mild Steel in HCl 1M, *Mor. J. Chem.,* 5(1). doi: 10.48317/IMIST.PRSM/morjchem-v5i1.6948

Eziuka J. E., Onyeachu B. I., Njoku D. I., Nwanonenyi S. C., Chidiebere M. A. Oguzie E. E., (2023) Elucidating the inhibition behaviour of Pterocarpussantalinoides leaves extract on mild steel corrosion in H_2SO_4 solution–GC-MS, FTIR, SEM, Experimental and computational approach, *Mor. J. Chem.,* 11(3). doi:10.48317/IMIST.PRSM/morjchem-v11i03.39198

Hooshmand Zaferani S., Sharifi M., Zaarei D. Shishesaz M. R., (2013) Application of eco-friendly products as corrosion inhibitors for metals in acid pickling processes – A review*, J. Environ. Chem. Eng.,* 1(4), 652-657. https://doi.org/10.1016/j.jece.2013.09.019

Huh J. H., Oh E. J. Cho J. H., (2005) Corrosion characteristics of electrochemically prepared phosphate doped polyaniline films in acidic chloride environments, *Synth. Met.,* 153(1-3), 13-16. doi: 10.1016/j.synthmet.2005.07.222

Itodoh U. E., Madufor I. C., Obidiegwu M. U. Oguzie E. E., (2023) Mollification of Mild Steel Corrosion in Hydrochloric Acid Solutions by Sodium carboxymethyl Cellulose and Polyethylene Glycol, *Mor. J. Chem.,* 11(2), 521-540. doi: 10.48317/IMIST.PRSM/morjchem-v11i2.38892

Ivankovic A., Martinez S. Soic I., (2016) Suppression of General and Localized Corrosion by Air-Dried TiO_2 Nanostructured Coatings on AISI 304 Stainless Steel, *Int. J. Electrochem. Sci.,* 11(9), 7660-7673. doi: 10.20964/2016.09.31

John S., Salam A., Baby A. M. Joseph A., (2019) Corrosion inhibition of mild steel using chitosan / TiO_2 nanocomposite coatings, *Prog. Org. Coat.,* 129, 254-259. https://doi.org/10.1016/j.porgcoat.2019.01.025

Lavanya C., Kusuma J. Geetha Balakrishna R., (2021) Pyrochlores: oxygen-rich moieties as ceramic fillers in uplifting the antifouling property and dye removal capacity of polymeric membranes, *Sep. Purif. Technol.,* 272, 118946-118955. https://doi.org/10.1016/j.seppur.2021.118946

Li L.-F., Caenen P. Celis J.-P., (2008) Effect of hydrochloric acid on pickling of hot-rolled 304 stainless steel in iron chloride-based electrolytes, *Corros. Sci.,* 50(3), 804-810. https://doi.org/10.1016/j.corsci.2007.09.006

Li L.-F., Caenen P., Daerden M., Vaes D., Meers G., Dhondt C. Celis J.-P., (2005) Mechanism of single and multiple step pickling of 304 stainless steel in acid electrolytes, *Corros. Sci.,* 47(5), 1307-1324. https://doi.org/10.1016/j.corsci.2004.06.025

Lopez D., Sanchez C. Toro A., (2005) Corrosion-erosion behavior of TiN-coated stainless steels in aqueous slurries, Wear, 258(1-4), 684-692. doi: 10.1016/j.wear.2004.09.015

Mohan S., Nair S. S., Ajay A. V., Senthil Saravanan M. S., Vishnu B. R., Sivapirakasam S. P. Surianarayanan M., (2020) Corrosion behaviour of ZrO_2-TiO_2 nano composite coating on stainless steel under simulated marine environment, *Mater. Today: Proc.,* 27, 2492-2497. https://doi.org/10.1016/j.matpr.2019.09.224

Movassagh-Alanagh F. Mahdavi M., (2020) Improving wear and corrosion resistance of AISI 304 stainless steel by a multilayered nanocomposite Ti/TiN/TiSiN coating, *Surf. Interfaces.,* 18, 100428-100467. doi: 10.1016/j.surfin.2019.100428

Mumtaz K., Takahashi S., Echigoya J., Zhang L., Kamada Y. Sato M., (2003) Temperature dependence of martensitic transformation in austenitic stainless steel, *J. Mater. Sci. Lett.,* 22(6), 423-427. doi: 10.1023/A:1022999309138

Nagarajan S. Rajendran N., (2009) Surface characterisation and electrochemical behaviour of porous titanium dioxide coated 316L stainless steel for orthopaedic applications, *Appl. Surf. Sci.,* 255(7), 3927-3932. https://doi.org/10.1016/j.apsusc.2008.10.058

Nazeer A. A. Madkour M., (2018) Potential use of smart coatings for corrosion protection of metals and alloys: A review, *J. Molec. Liq.,* 253, 11-22. https://doi.org/10.1016/j.molliq.2018.01.027

Nazeri A., TrzaskomaPaulette P. P. Bauer D., (1997) Synthesis and properties of cerium and titanium oxide thin coatings for corrosion protection of 304 stainless steel, *J. Sol-Gel Sci. Technol.,* 10(3), 317-331. doi: 10.1023/A:1018381503008

Nguyen S., Nakayama T., Takeda M. Takahashi T., (2020) Development of Yttrium Titanate/Nickel Nanocomposites with Self Crack-Healing Ability and Potential Application as Thermal Barrier Coating Material, *Mater. Trans.,* 61, 1510-1516. doi: 10.2320/matertrans.MT-MN2019006

Omar D., El Gouri M., Ebn Touhami M. El Harfi A., (2017) Evaluation of corrosion protection of epoxy coatings on copper during exposure to an aerated 3% NaCl solution, *Mor. J. Chem.,* 5(1). doi: 10.48317/IMIST.PRSM/morjchem-v5i1.5180

Onyeachu I. B., Solomon M. M., Adama K. K., Nnadozie C. F., Ahanotu C. C., Akanazu C. E. Njoku D. I., (2022) Exploration of the potentials of imidazole-based inhibitor package for heat exchanger-type stainless steel during acid cleaning operation, *Arab. J. Chem.,* 15(6), 103837. https://doi.org/10.1016/j.arabjc.2022.103837

Pantoja M., Velasco F., Abenojar J. Martinez M. A., (2019) Development of superhydrophobic coatings on AISI 304 austenitic stainless steel with different surface pretreatments, *Thin Solid Films,* 671, 22-30. https://doi.org/10.1016/j.tsf.2018.12.016

Perez F. J., Hierro M. P., Carpintero M. C., Gomez C. Pedraza F., (2002) Silicon/silicon oxide coating on AISI 304 stainless steel by CVD in FBR: analysis of silicides and adherence of coating, *Surf. Coat. Technol.,* 160(1), 87-92. doi: 10.1016/S0257-8972(02)00160-3

Boudalia M., Guenbour A., Bellaouchou A., Laqhaili A., Mousaddak M., Hakiki A., Hammouti B., Ebenso E.E. (2013) Corrosion Inhibition of Organic Oil Extract of Leaves of Lanvandula Stoekas on Stainless Steel in Concentrated Phosphoric Acid Solution, *Int. J. Electrochem.* Sci., 8 N°5, 7414-7424.

Ramaprakash M., Sreedhar G., Mohan S. Panda S. K., (2016) Corrosion protection studies of CeO_2–TiO_2 nanocomposite coatings on mild steel, *Transactions of the IMF,* 94(5), 254-258. doi: 10.1080/00202967.2016.1209892

Saif M., Shebl M., Mbarek A., Nabeel A. I., Maalej R. Shokry R., (2015) Synthesis of non-toxic phosphor material based on pyrochlore-type dititanate ($Eu^{3+}/Y_2Ti_2O_7$), *J. Photochem. Photobiol.* A, 301, 1-5. doi: 10.1016/j.jphotochem.2014.12.014

Salhi A., Bouyanzer A., El Mounsi I., Bendaha H., Chetouani A., Amhamdi H., Zarrouk A., Hammouti B., M.Desjobert J. Costa J., (2016) The inhibitive action of Pistacia lentiscus as a potential green corrosion inhibitor for mild steel in acidic medium, *Mor. J. Chem.,* 4(4). doi: 10.48317/IMIST.PRSM/morjchem-v4i4.6898

Salim A., Hamham S., Manni A., El mazouzi S. Naimi Y., (2023) Study of the inhibiting efficiency of the corrosion inhibitor (prop-2-yn-1-ol, methyloxirane) of mild steel in the chemical pickling (18.5% HCl), *Mor. J. Chem.,* 11(3). doi: 10.48317/IMIST.PRSM/morjchem-v11i3.39074

Samim P. M., Fattah-Alhosseini A., Elmkhah H. Imantalab O., (2020) Structure and corrosion behavior of ZrN/CrN nano-multilayer coating deposited on AISI 304 stainless steel by CAE-PVD technique, *J. Asian Ceram. Soc.,* 8(2), 460-469. doi: 10.1080/21870764.2020.1750102

Sikine M., Kandri Rodi Y., Elyoussfi A., Dafali A., Ouzidan Y., Kandri Rodi A., Ouazzani Chahdi F., Essassi E. M., Chetouani A., Hammouti B. Elmsellem H., (2018) New Corrosion inhibition of mild steel by 7-bromopyrido[2,3-b]pyrazine-2,3(1H, 4H)-dithiol in 1M hydrochloric acid solution, *Mor. J. Chem.,* 6(2). doi: 10.48317/IMIST.PRSM/morjchem-v6i2.11549

Verma C., Quraishi M. A. Ebenso E. E., (2020) Corrosive electrolytes, *Int. J. Corros. Scale Inhib.,* 9(4), 1261-1276. doi: 10.17675/2305-6894-2020-9-4-5

Xin S. S., Xu R. H., Yan H. T., Shen P. Li M. C., (2019) Electrochemical Corrosion Behaviour of Cerium Chemical Conversion Coatings on 304 Stainless Steel in Alkaline Solutions Containing Chloride Ions, *Int. J. Electrochem. Sci.,* 14(12), 11012-11018. doi: 10.20964/2019.12.84

Yang Z. Y., Wang J. Chen J. Y., (2008) Thermal-induced martensite transformation in 304 austenitic stainless steel, *Cailiao Rechuli Xuebao/Trans. Mater. Heat Treat.,* 29, 98-101.

Yu X., Bao W., Wang Q., Wang T., Su C., Zhang H. Hu W., (2022) Quantitative relationship between microstructure and optical properties of Er^{3+}-Yb^{3+} co-doped glass-ceramics containing pyrochlore-type crystalline phases, *Ceram. Int.,* 48(10), 13977-13986. https://doi.org/10.1016/j.ceramint.2022.01.282

Yu X., Zhao T., Wang T., Bao W., Zhang H. Su C., (2021) Up-conversion luminescence properties of Ho^{3+}-Yb^{3+} Co-doped transparent glass ceramics containing $Y_2Ti_2O_7$, *J. Non-Cryst. Solids, 574*, 121163-121171. https://doi.org/10.1016/j.jnoncrysol.2021.121163

Yue Y., Liu C. Jiang M., (2023) Formation and Evolution of Corrosion Product Film on 304 Stainless Steel in HCl-Based Pickling Solution under Chemical Oxidation, *J. Mater. Eng. Perform.,* 32(9), 3995-4004. doi: 10.1007/s11665-022-07390-3

Zhao H., Liu T., Bai Z., Wang L., Gao W. Zhang L., (2020) Corrosion behavior of 14Cr ODS steel in supercritical water: The influence of substituting Y_2O_3 with $Y_2Ti_2O_7$ nanoparticles, *Corros. Sci.,* 163, 108272-108281. https://doi.org/10.1016/j.corsci.2019.108272

Ziouche A., Hammouda A., Boucherou N., Mokhtari M., Hafez B., Elmsellem H. Abaidia S., (2021) Corrosion Protection Enhancement on Aluminum Alloy And Magnesium Alloy by Mo-CeO_2 conversion coating, *Mor. J. Chem.,* doi: 10.48317/IMIST.PRSM/morjchem-v9i3.27828